Resistance Feedback for Miniaturization of Shape Memory Alloys Actuators

Francesco Durante [1],*, Terenziano Raparelli [2] and Pierluigi Beomonte Zobel [1]

[1] Department of Industrial and Information Engineering and Economy (DIIIE), University of L'Aquila, P.le Pontieri 1, Località Monteluco, 67100 L'Aquila, Italy; francesco.durante@univaq.it (F.D.); pierluigi.zobel@univaq.it (P.B.Z.)

[2] Department of Mechanical and Aerospace Engineering (DIMEAS), Politecnico di Torino, Corso Duca degli Abruzzi 24, 10129 Torino, Italy; terenziano.raparelli@polito.it (T.R.)

* Correspondence: francesco.durante@univaq.it

Abstract: This paper illustrates an experimental activity for the closed-loop position control of an actuator made using shape memory alloy (SMA) wire. A solution with the self-sensing effect was implemented to miniaturize the systems, i.e., without external sensors. A proportional control algorithm was initially used, demonstrating the idea's feasibility: the wire can behave simultaneously as an actuator and sensor. An experimental investigation was subsequently conducted for the optimization of the developed actuator. As for the material, a Flexinol wire, Ni-Ti alloy, with a diameter of 0.150 mm and a length of 200 mm, was used. Preliminarily, a characterization of the SMA wire at constant and variable loads was carried out: the characteristics detected are elongation vs. electric current and elongation vs. electrical resistance. The control system is PC-based with a data acquisition card (DAQ). A drive board has been designed and built to read the wire's electrical resistance and power it by pulse width modulation (PWM). A notable result is that the actuator works with good precision and in dynamic conditions, even when it is called to support a load up to 65% different from that for which the electrical resistance-length correlation has previously been experimentally obtained, on which the control is based. This opens up the possibility of using the actuator in a counteracting configuration with a spring, which makes hardware implementation and control management simple.

Keywords: shape memory alloys; control; electrical resistance feedback; soft actuator

1. Introduction

Shape Memory Alloy (SMA) actuators have recently gained significant attention due to their unique capabilities in converting heat into mechanical energy. Their ability to recover their original shape after undergoing substantial deformation makes them suitable for use as actuators. Many works in the scientific literature propose using SMA as actuators [1–7]. Many scientific works concern their applications in many fields, such as micro-systems [8–11], robotics [12–19], biomedical [20–25], wearables [26–29], aerospace [30–34].

However, miniaturizing SMA actuators poses several challenges, including the need for precise control, compact design, and improved performance. One of the key factors influencing the performance of SMA actuators, in the form of wires, is their possibility to make a position control since, traditionally, they are used as on-off actuators. Position control is not easy in the open loop since the SMA deformation behavior is affected by the actual percentage of phase transformation from martensite to austenite, which depends on mechanical stress and the actual temperature affected by energy, thermal capacity, and heat transmission [35–37]. On the other hand, the closed loop, although a robust method for position control of actuators, needs additional hardware, such as sensors, to monitor the actual position and make it possible to send feedback to the controller. Nevertheless, sensors can be bulky and, in the case of our interest, can be prohibitive. For example, if we consider an SMA wire with a diameter of 0.15 mm, which is capable of a pull force of 3.3 N, which could potentially be a tiny actuator, it would lose its smallness if associated, for example, with a potentiometer. This was done in [38], where SMAs were implemented as actuators in a 3 DoF small

parallel robot where each actuator was made using a 150 μm diameter SMA wire. A resistive potentiometer, which has dimensions many times larger than the actuator's, was used for position control for each GDL: the ideal would be to have a sensor as small as the actuator.

Resistance feedback-based control techniques have emerged as a promising approach for enhancing the performance of miniaturized SMA actuators to address this challenge. By monitoring the resistance of the SMA wire or film during actuation, feedback control can be implemented to achieve higher precision and faster response times. This approach enables better control of the actuation force, position, and speed while improving efficiency. As mentioned above, for shape memory alloy wires, the deformation depends on the percentage of phase transformation, a function of the actual temperature that depends on many variables. However, it is possible to identify a link between the deformation and the electrical resistance being a bijection function (self-sensing effect). A link of this type can be used to get an estimate of the current length of the actuator. In these conditions, an SMA wire can perform the functions of the actuator and sensor at the same time.

Only some scientific works are related to implementing closed-loop SMA actuators using the self-sensing effect. Most implement the actuator drive through an analog system: these systems need, at the controller level, a DAC and, in the power section, an operational amplifier [39–43]. Although PWM control is frequently used to control general actuators, it has been little studied for SMA wire actuators with self-sensing effects. The authors in [44] proposed such a system by implementing proportional control. This approach is very convenient given that it requires straightforward hardware, which is present even on microcontrollers of minimal dimensions, as a digital port is sufficient. Meanwhile, the DAC, for processing analog signals, is a more sophisticated component and is only sometimes present on microcontrollers. Even a simple transistor can perform the power function, while an operational amplifier is needed with analog signals. To the authors' knowledge, the same control approach, using the self-sensing effect via PWM signal, is proposed in two other works. In these works, the model linking the actual deformation to the electrical resistance is expressed in a mathematical form depending on 7 [45] or 8 [46] coefficients.

This paper presents the application of SMA wires as actuators with feedback control and self-sensing effect, with PWM drive, using a simple linear type deformation - electrical resistance model, i.e., expressed by a first-degree polynomial.

The actuator is an SMA wire coupled with springs or masses with antagonistic functions. The electrical resistance-length relationship was carried out after the electric current-strain and the electric resistance-strain characterization. Then, a proportional control was implemented. Subsequently, optimization was carried out through experimental tests aimed at highlighting the influence of different components of the control logic, i.e., proportional (P), derivative (D), integral (I), and their combinations. Also, the parameters of the PWM command and the influence of the acting antagonist force were investigated.

2. Materials and Methods

2.1. Shape memory alloy wires: experimental characterization

In shape memory actuators, it is possible to implement feedback control without using dedicated sensors by exploiting a characteristic of these alloys known as the self-sensing effect, which allows you to link the deformation of the actuator to its electrical resistance.

The resistance vs. length trends, with respect to temperature, show a strong hysteresis; on the contrary, the relationship that binds them together is almost free from this phenomenon, and if we exclude the two extreme phases of the transformation of the material (completely martensite or austenite), it can theoretically be considered linear, Figure 1.
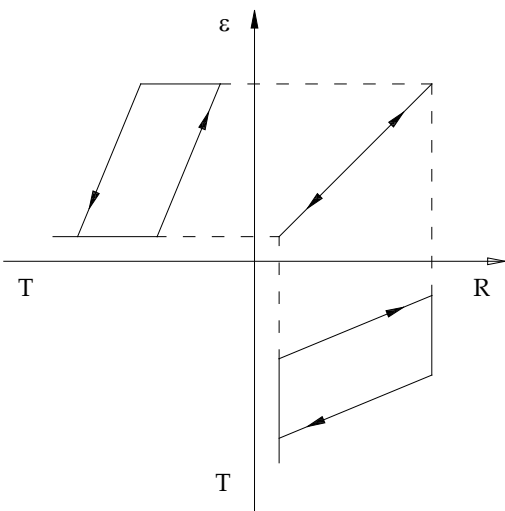
Figure 1. Characteristic deformation-resistance, resistance-temperature, and deformation-temperature.

To understand the phenomenon described, various experimental characterizations were carried out on shape memory alloy wires to identify a link between deformation and other measurable functional parameters to estimate the current deformation of the wire starting from measurements of other variables. In particular, constant load and variable load strain tests were conducted in which strain and electric current were measured. Subsequently, another test campaign aimed to determine the link between deformation and the wire's electrical resistance under constant and variable load.

2.1.1. Test bench

The thread under test is a commercial one, Flexinol brand, type 150 HT, whose characteristics are shown in Table 1, with a length of 200 mm.

Table 1. Technical specification of the wire.

Flexinol 150HT
Wire diameter: 150 μm
Linear resistance: 50 Ω/m
Maximum recovery force: 10.4 N
Recommended deformation ratio: 3-5 %
Activation start temperature: 68°C
Activation finish temperature: 78°C
Relaxation start temperature: 52°C
Relaxation finish temperature: 42°C

To determine the deformation of the wire, the measuring bench visible in Figure 2 was created in two versions, "a" and "b," the "a" for the constant load tests and the "b" for the variable load ones. The bench consists of an upright (an aluminum profile with a rectangular section measuring 80×40×600mm) on which the supports of the various components are connected using screws, that is:

- a base 1, where the electrical connections and the lower wire fixing system are shown;
- a pulley 2 that serves as a return for the application of the payload and to which the index for reading the movement of the free end of the wire is connected jointly;
- the graduated scale 3.

    In the case of variable load tests, carried out with the opposition of a spring, there is also:

- Support spring fixing system 4, which allows preload adjustment.

The wire is connected at the bottom to the base and at the top to a Kevlar cord 5 that engages the pulley and carries the paying load to the other end. The connections between these are made through eyelets and mini hooks; in particular, the eyelets are attached to the wire by the manufacturer's " clamps. " Both the eyelets and the hooks are made of metal; in this way, it was possible to make the electrical connections on the hooks, allowing easy wire replacement. The material of the connecting cord was chosen due to its mechanical properties in the length direction, Table 1, and the low resistance in the transverse direction; in particular, the specific tensile modulus of elasticity (modulus of elasticity/density) is more than three times that of steel. These features protect you from any cord influences on the measuring chain. The pulley transforms the linear displacement of the free end of the wire into index rotations. At the same time, the graduated scale has been divided to read the linear displacement of the wire directly. The whole of the measurement chain has been designed in such a way as to have an amplification of the displacements of a factor of 10. Since the system has proved to be sensitive to external conditions, particularly air currents, everything has been inserted inside a transparent Plexiglas tube.

(**a**)   (**b**)
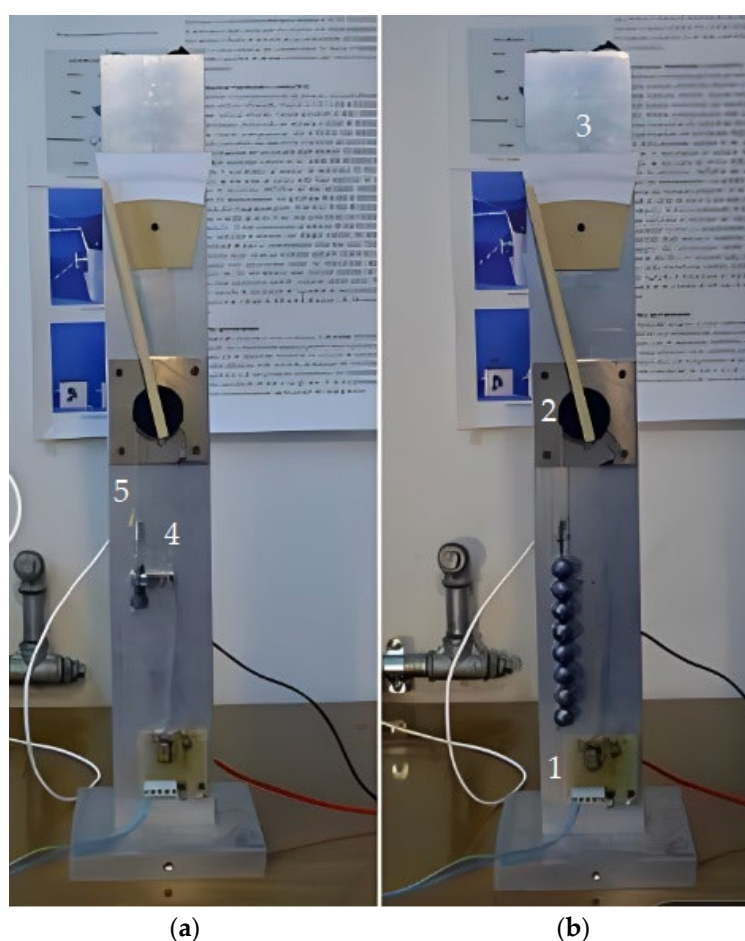
Figure 2. Measurement bench: arrangement for antagonist force by the spring (**a**); arrangement for the antagonist force by weights (**b**).

2.1.2. Electric current-strain curves

The first investigations help acquire sensitivity, have a complete picture of shape memory alloys' behavior, and evaluate the possibility of creating simple open-loop control systems. This activity led to the measurement of a series of current-strain curves obtained at constant and variable loads. The circuit in Figure 3 has been created by which it is possible to vary the voltage applied to the ends of the wire and to read the intensity of the current flowing through it.
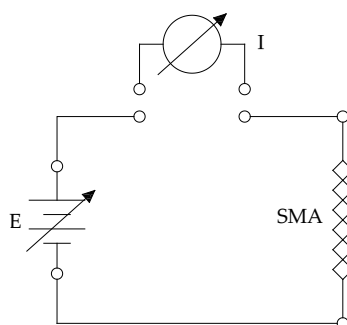
Figure 3. Measurement circuit.

Using this circuit, together with the bench in Figure 2, allows us to derive the link between the deformation of the wire and the current flowing through it. All the test sessions were conducted in almost stationary conditions: the power supply voltage was varied in small "steps," and the system stabilization was waited for with each variation. For ease of use, the experimental data are reported as a function of the percentage shortening (ε%):

$$\varepsilon\% = \frac{shortening}{initial\ length}\,100 \tag{1}$$

Constant load characterization

In this case, the payload consists of weights (the curves are obtained with a total load of 1.50 N), limiting the recovery of the actuator to a value equal to 3.5%. Two of the curves obtained are shown in Figure 4.
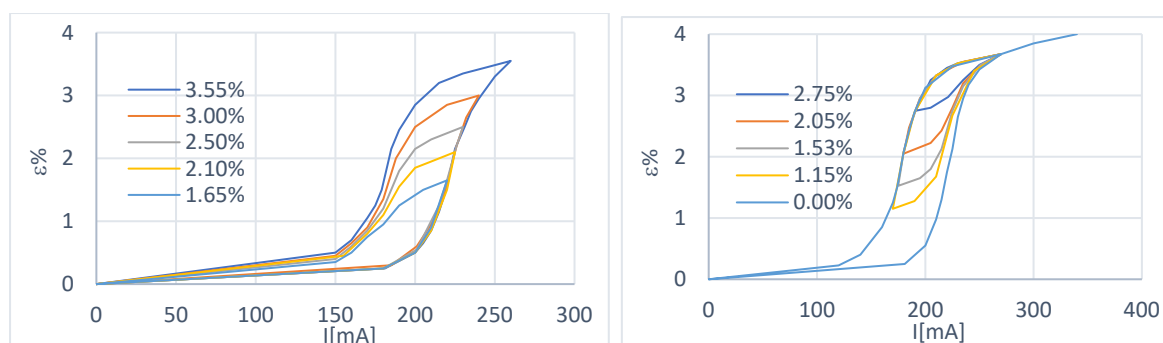
Figure 4. First-order sub-cycles of the deformation-current characteristic at constant load. Starting from an initial state of 100% martensite (left) and starting from an initial state of 100% austenite (right).

Variable load characterization

Depending on the characteristics of the wire provided by the manufacturer, the tests were carried out in such a way as to have a maximum deformation of 3,5%, with a maximum load of 3.3 N and a recovery load (minimum) of 0.70 N. The above values have been adjusted for the spring preload. The results are shown in Figures 5-6.

Some considerations can be made from the curves obtained:

1. in the case of constant load at a deformation recovery of 3.5%, the wire has yet to reach the condition of complete austenitization; this is evidently due to the more significant deformation to which it is subjected in cooling. In fact, with the use of the spring, it is possible to choose the extent of the deformation with an appropriate adjustment of the preload, while in the case of constant load, there is a return load (in our case, it is the paying load) more significant than the recovery load of the wire and this causes an over-deformation;
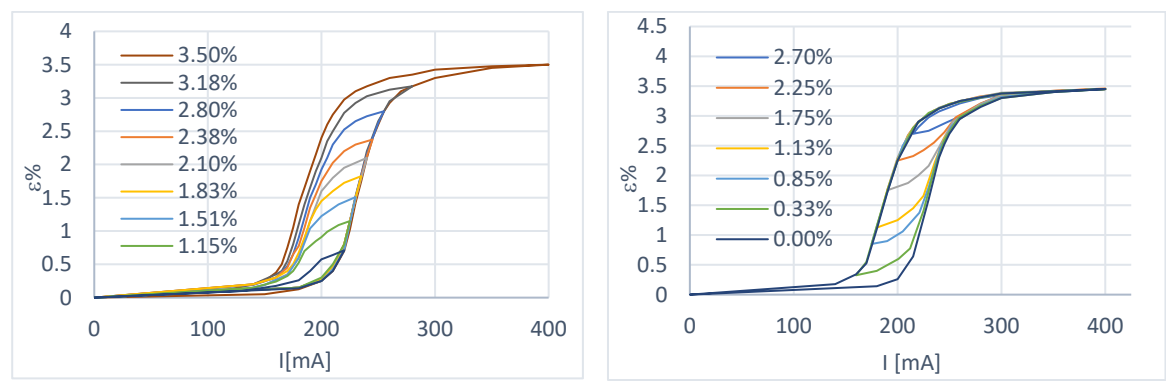
Figure 5. First-order sub-cycles of the deformation-current characteristic at variable load. Starting from an initial state of 100% martensite (left) and starting from an initial state of 100% austenite (right).
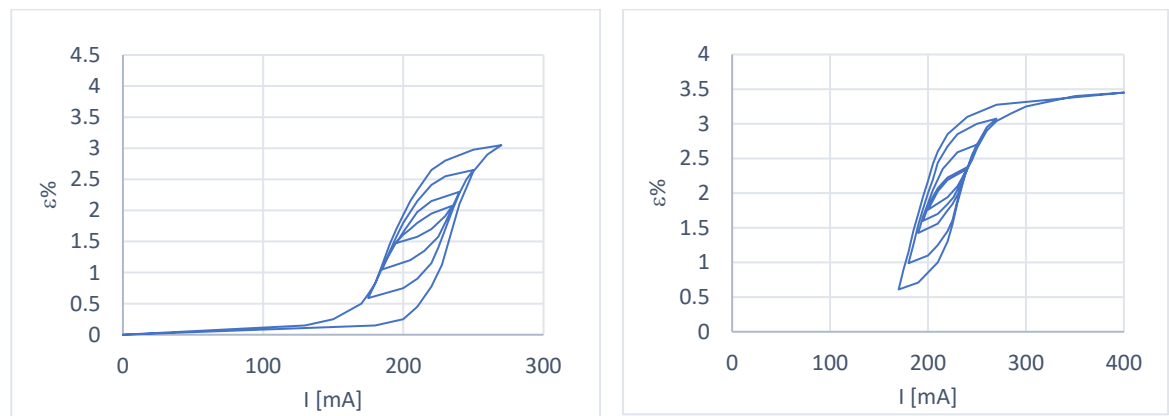
Figure 6. Multiple sub-cycles of the deformation-current characteristic at variable load. Starting from an initial state of 100% martensite (left) and starting from an initial state of 100% austenite (right).

2. The transformation interval is wider in the case of variable load because a deformation recovery value of 3.5% corresponds to a load of 3.3 N, which is more significant than in the case of constant load tests. This shows the dependence of the amplitude of the transformation interval on the applied load;
3. there is excellent repeatability of the behavior when moving on the primary hysteresis cycle;
4. reaching a position starting from a condition other than 100% Austenite or 100% Martensite becomes complex, Figure 6;
5. Figure 7 shows two primary hysteresis cycles obtained at different times; we note the translation of the curve due to the different environmental conditions (different external temperatures).

One thing not visible in the curves is the strong sensitivity of the system to the presence of air flows.
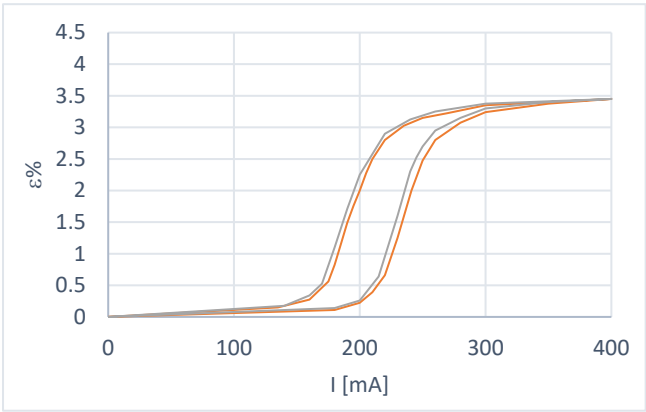
Figure 7. Comparative analysis between two variable load test sessions.

2.1.3. Electric resistance-strain curves

These curves were obtained using the measuring bench in Figure 2 and the circuit in Figure 8. The resistance is calculated with Ohm's law (R = V / I) by directly reading the values of the current passing through the wire and the potential difference established across it.
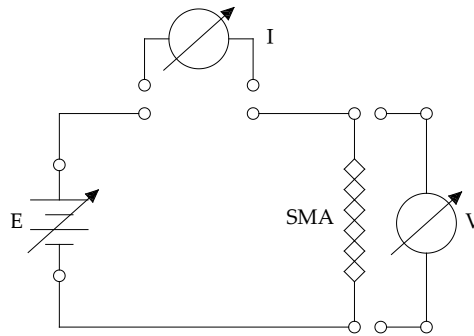
Figure 8. Circuit for determining the electrical resistance of the SMA wire.

Variable load characterization

The deformation-resistance characteristic (ε-R) was obtained under variable load conditions, following the procedure illustrated to determine the ε-I curves. Two results of the test sessions are shown in Figure 9.
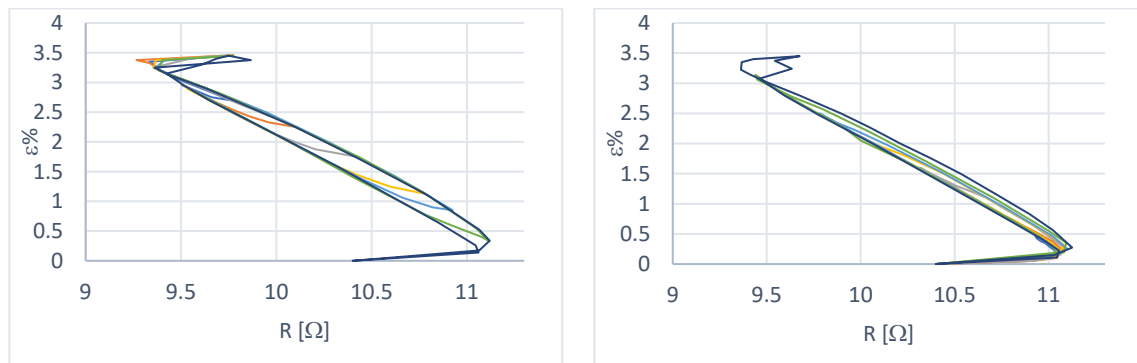
Figure 9. First-order hysteresis sub-cycles with variable load start from 100% Austenite (left) and start from a state of 100% Martensite (right).

Constant load characterization

The constant load deformation-resistance characteristic, shown in Figure 10, was obtained with a load of 2.0 N. It also shows the trend line obtained by excluding the extremes of transformation. The load of 2.0 N represents a possible payload supported by the actuator.
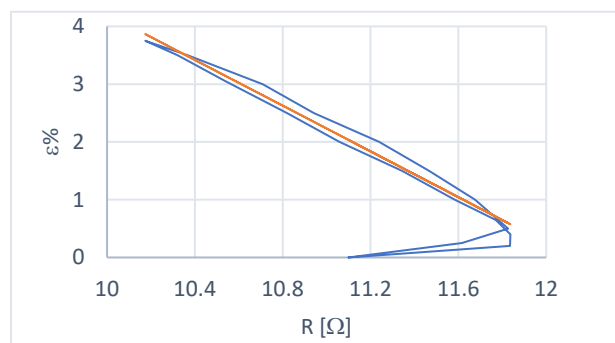
Figure 10. Constant load characteristic and trend line.

The data obtained show that:

1. the ε-R characteristic is not free from hysteresis phenomena. The amplitude of the cycle is, however, significantly lower than that of the ε-I characteristic;
2. the mean curve of the cycle, excluding the extremes of the transformation, can be considered linear;
3. the data are characterized by good repeatability on the external hysteresis cycle;
4. Providing a one-to-one deformation-resistance relationship at the extremes of the transformation interval is impossible.

2.2. Control with self-sensing

From the above data, it can be concluded that the current-deformation curves cannot be used to estimate the actual length of the wire since the marked hysteresis and the abrupt trend of the graphs, which is non-linear, make it impossible to identify a precise value of the deformation starting from by the electric current flowing through the wire. At the same time, the characteristic electrical resistance-deformation presents a more gradual, linear trend and a significantly reduced hysteresis. From the graphs, both at variable and constant loads, it is immediately evident that it is possible to identify a one-to-one correspondence between electrical resistance and deformation for a large section of the graph. These curves were used to implement the actuator position control. In particular, the position control with constant load has been implemented. The idea is to create a control cycle that provides, in succession, the power supply to the actuator to make it contract and, subsequently, to interrupt the power supply for a very short time to measure the actual electrical resistance to rise through the detected characteristic, to the actual length and to implement feedback in a continuous cycle. The SMA wire is thus found to perform alternatively the functions of the actuator and sensor.

Power is delivered via a Pulse Width Modulation (PWM) signal; the electrical resistance of the actuator is obtained by reading the voltage drop across the SMA wire and a known resistance according to the scheme in Figure 11.
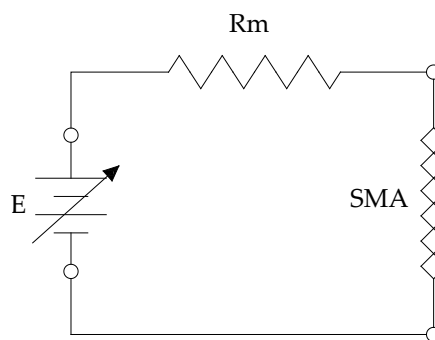
Figure 11. Wire electrical resistance measurement circuit diagram.

The resistance of the SMA wire is estimated with the relationship:

$$Rsma = \frac{Vsma}{Vm} \cdot Rm \tag{2}$$

The model for estimating the actual deformation from the electrical resistance is in (3).

$$\varepsilon = 0.043 - 0.00804\ R \tag{3}$$

2.2.1. Control architecture

Figure 12 shows a block diagram of the control system.
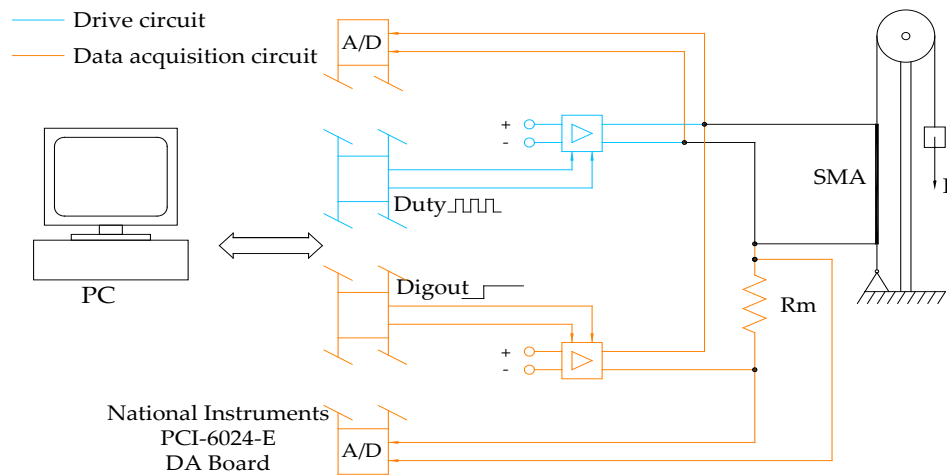
Figure 12. Functional diagram of the control system**.**

There are four parts.

1. The characteristics of the actuator (the SMA wire) are shown in Table 1.
2. The drive is the power circuit equipped with the electrical and electronic components that allow the actuator to be powered.
3. The measurement circuit is based on the diagram in Figure 11, which determines the length of the actuator.
4. A PC, in which the control algorithms reside, with a National Instruments PCI-6024E data acquisition card for interfacing PC and drive and measurement unit.

In the embodiment, the drive and measurement circuits are mounted on a homemade board but constitute two independent sections, Figure 13.

Each of the two circuits consists of:
- a 4N33 optocoupler used to separate, from an electrical point of view, the control part from the power part to avoid possible damage to the data acquisition card;
- a BC288 transistor which enables the transit of the power signal;
- a polarization resistance (Rp);
- a resistance on the control branch (Rc) used to lower the voltage across the optocoupler;
- on the measurement circuit, there is the resistance Rm, which is necessary to determine the resistance of the wire in SMA.

The value of the polarization resistance (Rp = 1 kΩ) was chosen according to the optimization of the circuit response times, and the value of 1 kΩ was adopted, as it also allows you to limit the current in the optocoupler.

The PWM signal for enabling the passage of power to the actuator has a base frequency of 30 kHz, and the power circuit has a response time of less than one ten-thousandth of a second.

(a) **(b)**
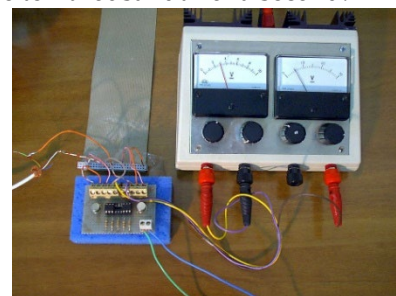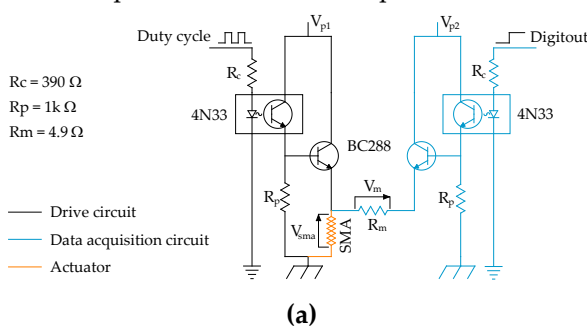
Figure 13. The electric scheme of the board used for the measurement of the electrical resistance and the driving of the actuator (a). The physical homemade board (b).

2.2.2. Control algorithms

The explanatory scheme of the control logic adopted is visible in Figure 14.
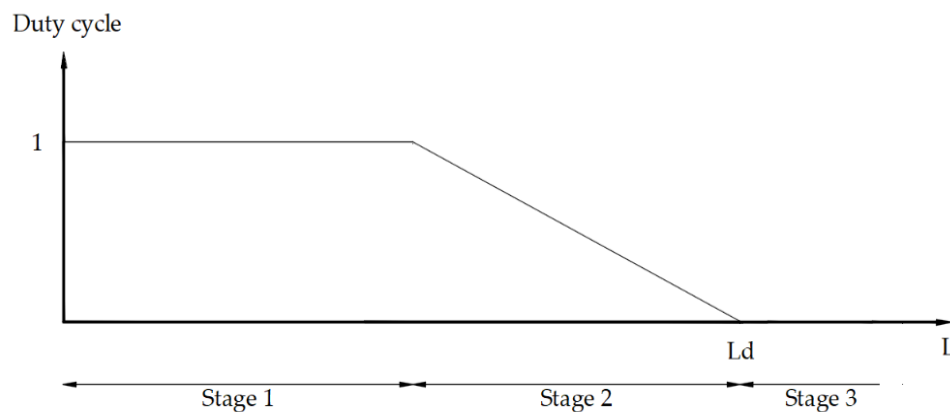
Figure 14. Control logic scheme: in stage 1, far from the target, the control supplies the maximum power. In stage 2, close to the target, the control becomes proportional. Stage 3, overcoming the target, the control cuts power off.

Three phases are recognized:
1. when the actuator is far from the desired deformation value (phase 1), the control sends the maximum possible power (duty cycle = 1);
2. when the actuator is close to the desired deformation (phase 2), the control becomes proportional (P);
3. if the actuator exceeds the desired shortening (phase 3), the power supply is cut off, and the recall load provides for the deformation (elongation) of the actuator.

This control logic allows a faster approach phase than a purely proportional one.

To read the voltages with which to trace the deformation of the actuator, the power and measurement circuits are powered alternately according to the following cyclic sequence:
1. the power circuit is activated;
2. the power circuit is deactivated;
3. the measurement circuit is activated;
4. the voltages are read;
5. the measuring circuit is deactivated.
6. Phases 3-5 have an overall duration equal to 2.2% of the total operating time.

2.2.3. Experimental validation

To conduct the experimental tests, a measurement chain was created, which supports the developed system and allows you to measure the displacements of the actuator and compare them with the desired ones. It consists of:
- a National Instruments PCI-6034E data acquisition card;
- a PC where the card management program resides;
- a position transducer.

Figure 15 shows the experimental setup scheme.
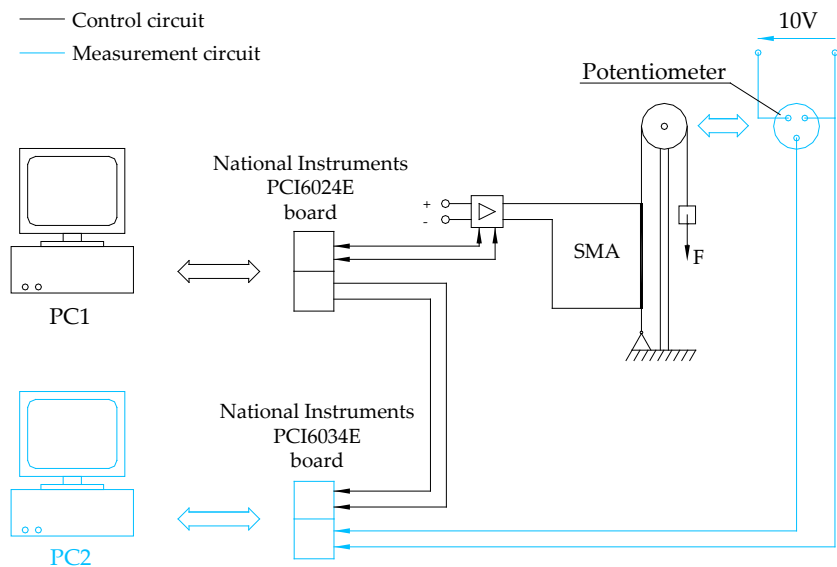
Figure 15. Experimental setup scheme**.**

The measurement sensor is a servo potentiometer suitable for use with precision DC motors or as a position transducer. The contacts are multi-brush and guarantee a high resolution. Two bearings reduce friction to a minimum and require a low torque for shaft rotation. Table 2 shows the characteristics of the potentiometer.

Table 2. Characteristics of the potentiometer**.**

Vishay 157
Maximum current on contacts: 10 mA
Electric rotation angle: 340° ± 4°
Mechanical rotation angle: 360°
Starting torque (max): $28 \cdot 10^{-4}$ Nm
Torque at steady state (max): $21 \cdot 10^{-4}$ Nm
Supply voltage (max): 10V
Maximum electrical resistance: 10 kOhm

The pulley for the recovery load has been mounted on the axis of the potentiometer, Figure 16.
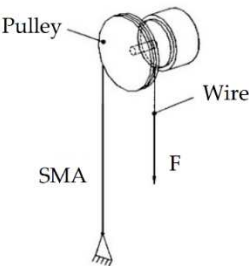
Figure 16. The pulley mounted on the axis of the potentiometer**.**

The power supply is set at 10 V to make the most of the transducer's sensitivity available. The Vinit values (voltage supplied by the potentiometer in zero conditions) and the proportionality constant of the transducer (Kt) are shown below:

- Vinit = 3.127V
- Kt = 0.1V / mm.

The control program of the board provides for the timed reading of the voltage value of the potentiometer at regular intervals of 0.1 seconds. The card is enabled for reading through a consent signal sent by the wire control system, and the connection is made through a digital channel. When the board detects voltage on this channel, it starts reading the potentiometer, which ends when the signal returns to zero. The consent signal allows the reference and position signals to have the same time base.

3. Results

3.1. Performance with proportional control

Experimental tests were conducted for real-time control of the position of the developed actuator. The performances were investigated for step, Figure 17, ramp, Figure 18, and sinusoidal-type inputs, Figure 19.
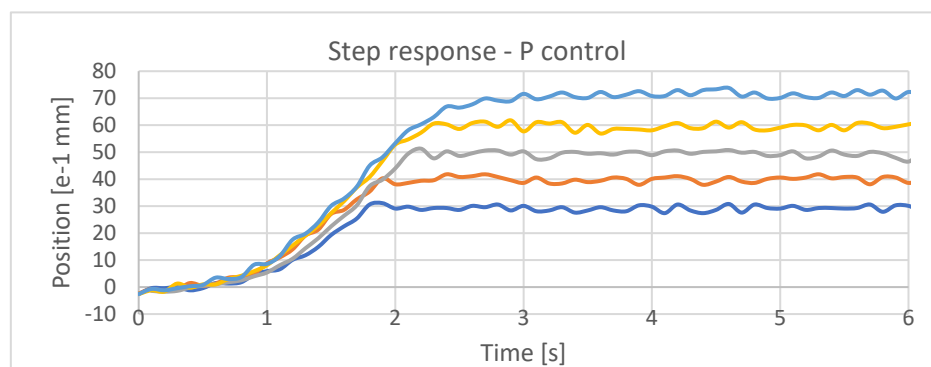
Figure 17. Step responses for the target ranging from 0.3 mm to 0.7 mm**.**
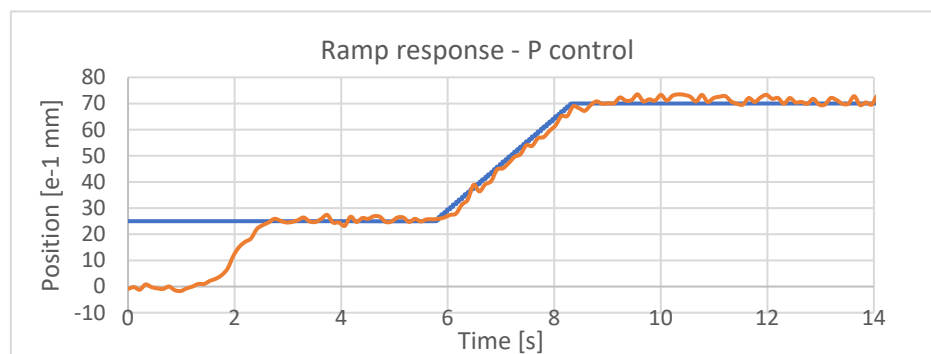
Figure 18. Ramp response for a target of 0.7 mm**.**
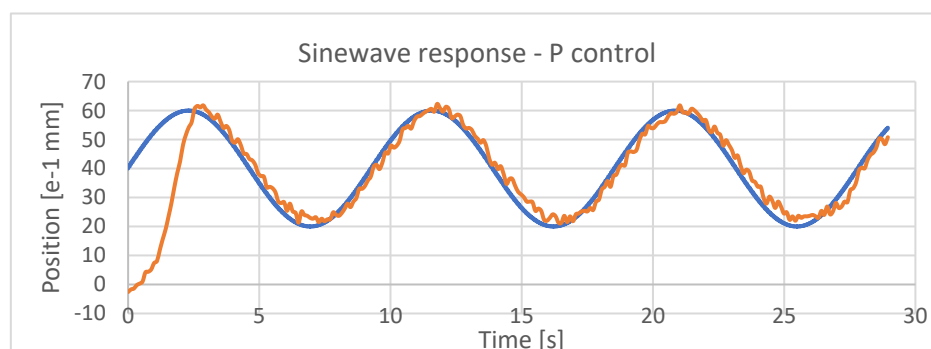
Figure 19. Response for a sinewave with a mean value of 0.4 mm, amplitude of 0.2 mm, period of 9 s.

The onset of vibrations around the reference position reached by the actuator can be noted despite good behavior in getting the assigned position.

The same behavior type is found in variable references such as the RAMP or the SINUSOIDAL trajectory.

3.2. Performance after Optimization

The need to obtain a more stable positioning around the desired position has led to analyzing the causes of the vibrations and identifying possible solutions according to those parameters that could significantly influence the system.

All those variables, from the control logic to the various functional parameters that could improve the response, were considered.

Attention was mainly focused on three aspects that primarily seemed to affect the behavior of the system:

- The control logic
- The actuator power signal (PWM)
- The return force exerted on the wire

Tests were conducted by varying each of the parameters described above from time to time to identify the possible optimal combinations that would improve the performance of the control.

As regards the control logic, it was decided to move from a purely Proportional to a Proportional-integral - Derivative (PID) control and also to experiment with the behavior of the different combinations: Proportional - Derivative (PD), Proportional - Integrative (PI).

We also worked on the signal that feeds the PWM SMA wire, having noticed evident effects of the square wave frequency that characterizes the input signal. Also, in this case, proceeding experimentally, it was possible to identify the optimal values to be assigned to this parameter.

Finally, we intervened on the return force acting on the wire by applying weights of different values since, from preliminary tests, it was found that the variation of the force resistant to the movement of the actuator affects the quality of the system's response.

As regards the calibration of the control parameters, we proceeded with the Ziegler-Nichols criterion, obtaining the values shown in Table 3, while in Table 4, the optimization experimental plan is presented.

Table 3. Control parameters used in the experimental tests.

	K_p	T_i	T_d	K_i	K_d
P	0.3				
PI	0.27	2.55		0,10	
PID	0.37	1.7	0.425	0,21	0,16

Table 4. Optimization experimental plan.

Control	Load	Rate
P	2.0 N	30kHz
PI	2.5 N	110 kHz
PID	3.0 N	130 kHz

The control system has been tested for different types of input references:

- Step entrances;
- Ramp trajectory tracking;
- Sinusoidal trajectory tracking.
- Response to external disturbance.

Figure 20 presents the responses to steps input for a combination of the tested parameters. In Figures 21–23, the responses to steps input, ramp input, and sinusoidal input for the optimized

combination of the tested parameters are presented, respectively. In Figure 24, the response to a disturbance consisting of a current of fresh air is shown.
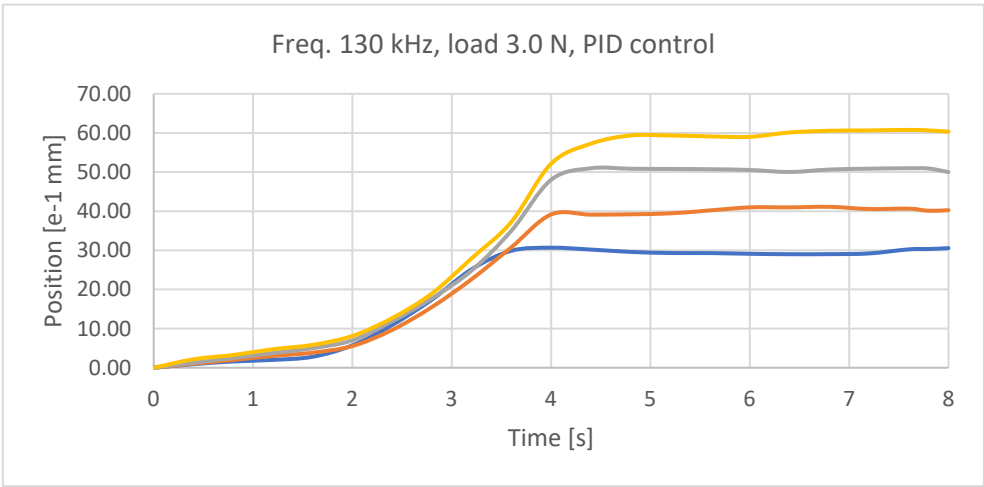
Figure 20. Step responses for the target range from 0.3 mm to 0.6 mm for a combination of experimented parameters.
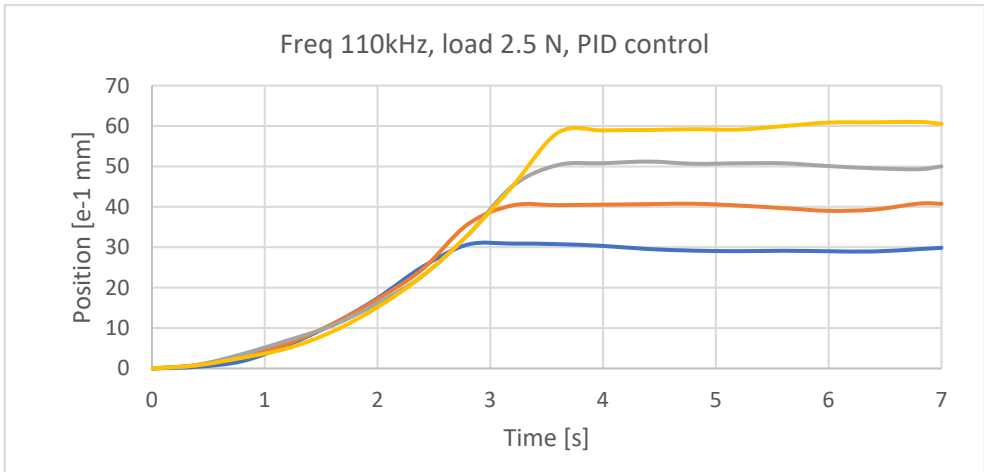
Figure 21. Step responses for the target ranged from 0.3 mm to 0.6 mm after optimization.
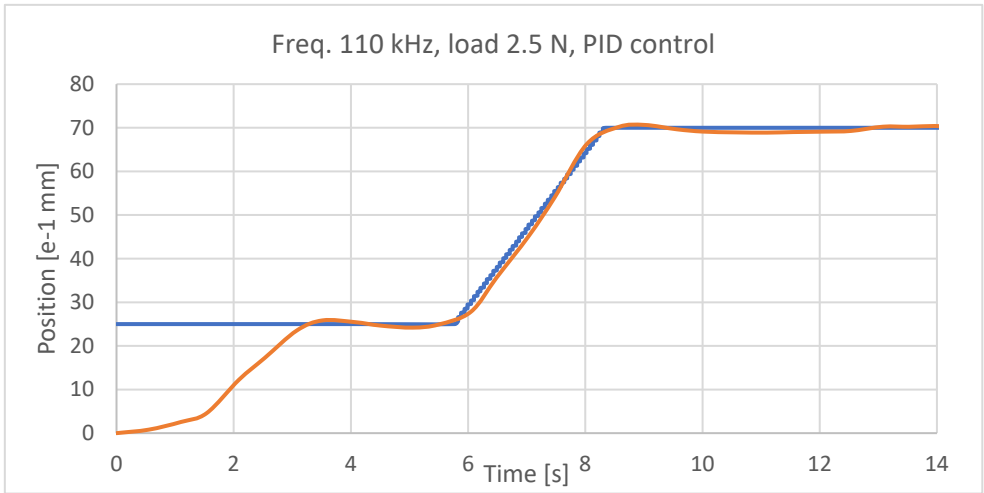
Figure 22. Ramp response for a target of 0.7 mm after optimization.
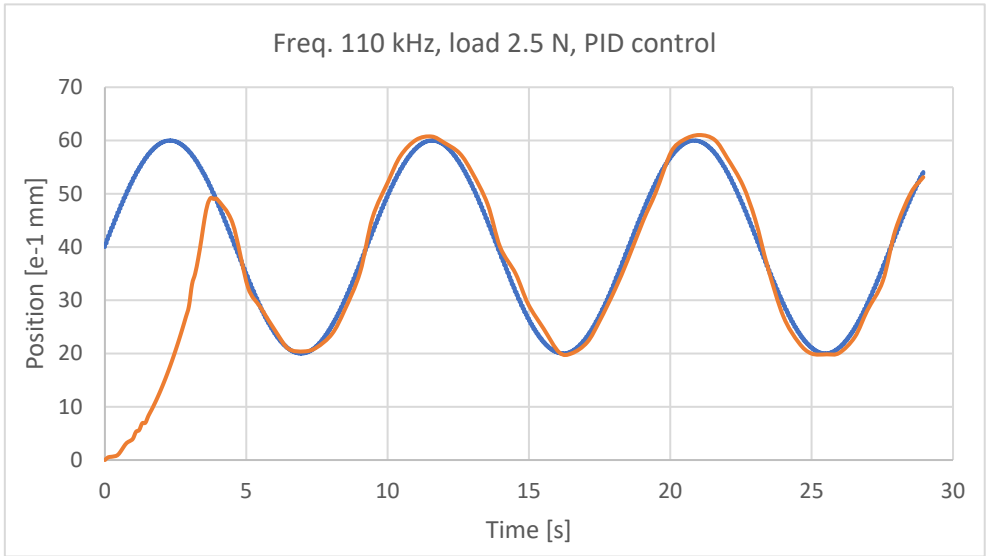
Figure 23. Response for a sinewave with the mean value of 0,4 mm, amplitude of 0,2 mm, and period of 9 s after optimization.
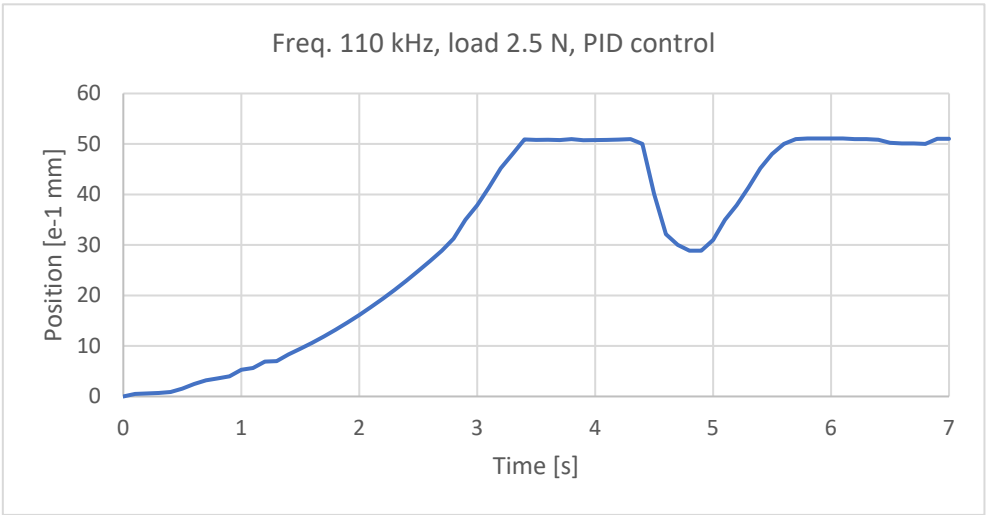
Figure 24. Response to a disturbance at 4.4 s**.**

4. Discussion

To evaluate and compare the performance of the different systems as the configurations vary, the following indicators have been identified:

- Max and Min's values reached in positioning;
- fluctuation % = $\frac{Max-Min}{stroke} \cdot 100$;
- Average value.

By "stroke," it has to mean the maximum stroke of the actuator equal to 7.5 mm.
The values obtained are summarized in Tables 5-7.

Table 5. Test with: Load 2,0 N, Rate 30kHz, P control.

	Ref. 20	Ref. 30	Ref. 40	Ref. 50	Ref. 60	Ref. 70
Max [10^{-1} mm]	22.3	30.8	41.8	50.8	61.3	73.8
Min [10^{-1} mm]	17.6	27.4	37.9	46.5	56.9	69.6
fluctuation %	6.2	4.5	5.2	4.5	5.8	5.6
Mean [10^{-1} mm]	19.7	29.1	39.8	49.4	59.4	71.4

Table 6. Test with: Load 2,5 N, Rate 110kHz, PID control.

	Ref. 30	**Ref. 40**	**Ref. 50**	**Ref. 60**
Max [10^{-1} mm]	30.98	41.40	51.20	61.18
Min [10^{-1} mm]	29.32	38.96	48.96	58.87
fluctuation %	2.21	3.25	2.99	3.08
Mean [10^{-1} mm]	30.38	39.81	50.16	

Table 7. Test with: Load 3,0 N, Rate 130kHz, PID control.

	Ref. 30	**Ref. 40**	**Ref. 50**	**Ref. 60**
Max [10^{-1} mm]	30.87	40.80	51.02	61.13
Min [10^{-1} mm]	28.88	38.76	48.78	59.09
fluctuation %	2.65	2.72	2.99	2.76
Mean [10^{-1} mm]	29.98	39.19	49.94	59.87

Based on the experimental results, the following observations can be made. As for the PWM control signal frequency, this value was initially set to 30 kHz.

An increase in the frequency value corresponds to a less reactive response of the actuator once the desired position has been reached. By further increasing the value of this parameter, a situation is reached in which the system becomes insensitive to the control; the position reached is the full-scale position regardless of the set reference value.

The recovery force influences this parameter: with the initial value of 2.0 N, the contraction of the wire is very rapid. By increasing it, the frequency can be set to increasingly higher values. The limit value for the frequency of the control signal, applying a restoring force of 2.0 N, is approximately 100 kHz, with a force of 3.0 N, it is possible to reach frequencies of about 130 kHz. The maximum working recovery force that can be used relates to the yield strength of the Nitinol 150HT wire, equal to 190 MPa, i.e. 3.3 N.

The increase in the counteracting force led to a reduction in the amplitude of the oscillations; at the same time, the system's response times increased: with a weight of 3.0 N, there were delays in the positioning of approximately 2 seconds. A good compromise between response times and vibration attenuation was achieved by applying weights of 2.5 N. It should be noted that although the system was not characterized according to the different weights applied, the same Resistance-Deformation curve was used, and the results obtained are still satisfactory.

Regarding the control type, a Proportional - Derivative control system was considered after implementing proportional control. However, control of this type cannot guarantee precise positioning, so an integrative component was added to eliminate the error when fully operational. Introducing a P.I.D control does not eliminate vibrations but is still advantageous for good precision and robustness of the system. In particular, obtaining a good response for position values smaller than those achievable with the proportional system was possible. It was possible to reach the 20 position on the graduated scale, corresponding to a 2 mm shortening of the SMA wire.

The optimal combination of the parameters illustrated above was the following:

Square wave frequency: 110 kHz;
Recovery/applied force: 2.5 N;
Control type: P.I.D.

Furthermore, the parameter that most seems to affect the unstable behavior of the SMA actuator is the frequency of the PWM activation signal.

5. Conclusions

The paper presents the development of an SMA wire actuator with feedback position control using the self-sensing effect for estimating the actual length of the actuator. From a hardware point of view, the system has been implemented using electronic components with very simple operation

thanks to the PWM-type control signal. A digital port at the controller level and a transistor in the power section are sufficient. As regards the model that links the deformation of the wire to the electrical resistance, a model obtained experimentally, and which can be expressed through a simple linear law, was used. The actuator can work in an agonist-antagonist configuration with weights or with a spring. A proportional type control has been implemented, and it presents oscillations. Subsequently, experimental research was carried out to find the optimal configuration considering the control logic components, the PWM command parameters, and the influence of the counteracting force. After parameter optimization, there was a reduction in the amplitude of the oscillations of approximately 35%. However, steady-state fluctuations are present, but the positioning was carried out with an accuracy approximately below 2.5%; the frequency is reduced from around 10 Hz to 1 Hz, resulting in much smoother behavior. The optimal configuration is the one in which a P.I.D. control is implemented, with a PWM signal frequency equal to 110,000 Hz and a counteracting force equal to 2.5 N.

The result is an actuator well-suited to miniaturized systems and even drivable by a tiny controller and driver.

Author Contributions: Conceptualization, FD; methodology, FD, PBZ, and TR; validation, FD; formal analysis, FD, PBZ, and TR; investigation, FD, PBZ, and TR; data curation, FD; writing—original draft preparation, FD; writing—review and editing, FD; visualization, FD, PBZ and TR; supervision FD, PBZ and TR. All authors have read and agreed to the published version of the manuscript.

Data Availability Statement: Not applicable.

Acknowledgments: The authors would like to acknowledge the support given by Eng. Tito Avalle for his contribution to the experimental activity.

Conflicts of Interest: The authors declare no conflict of interest.

References

1. Kittinanthapanya, R.; Sugahara, Y.; Matsuura, D.; Takeda, Y. Development of a Novel SMA-Driven Compliant Rotary Actuator Based on a Double Helical Structure. Robotics 2019, 8(1), 12; https://doi.org/10.3390/robotics8010012.
2. Britz, R.; Motzki, P.; Seelecke, S. Scalable Bi-Directional SMA-Based Rotational Actuator. Actuators 2019, 8(3), 60; https://doi.org/10.3390/act8030060.
3. Copaci, D.; Blanco, D.; Moreno, L. Flexible Shape-Memory Alloy-Based Actuator: Mechanical Design Optimization According to Application. Actuators 2019, 8(3), 63; https://doi.org/10.3390/act8030063.
4. Schmelter, T.; Theren, B.; Fuchs, S.; Kuhlenkötter, B. Development of an Actuator for Translatory Movement by Means of a Detented Switching Shaft Based on a Shape Memory Alloy Wire for Repeatable Mechanical Positioning. Crystals 2021, 11(2), 163; https://doi.org/10.3390/cryst11020163.
5. Ballester, C.; Copaci, D.; Arias, J.; Moreno, L.; Blanco, D. Hoist-Based Shape Memory Alloy Actuator with Multiple Wires for High-Displacement Applications. Actuators 2023, 12(4), 159; https://doi.org/10.3390/act12040159.
6. Durante F., Beomonte Zobel P., Raparelli T. The experience at University of L'Aquila on shape memory alloys actuators. (2018) Mechanisms and Machine Science, 49, pp. 638 - 645. DOI: 10.1007/978-3-319-61276-8_67
7. Dauksher, R.; Patterson, Z.; Majidi, C. Characterization and Analysis of a Flexural Shape Memory Alloy Actuator. Actuators 2021, 10(8), 202; https://doi.org/10.3390/act10080202.
8. Raparelli T., Zobel P.B., Durante F. A proposed methodology for the development of microgrippers: An application to a silicon device actuated by shape memory alloy wires. (2018) International Journal of Mechanical Engineering and Technology, 9 (2), pp. 235 - 249.
9. Zainal, M.; Sahlan, S.; Ali, M. Micromachined Shape-Memory-Alloy Microactuators and Their Application in Biomedical Devices. Micromachines 2015, 6(7), 879-901; https://doi.org/10.3390/mi6070879.
10. Garcés-Schröder, M.; Hecht, L.; Vierheller, A.; Leester-Schädel, M.; Böl, M.; Dietzel, A. Micro-Grippers with Femtosecond-Laser Machined In-Plane Agonist-Antagonist SMA Actuators Integrated on Wafer-Level by Galvanic Riveting. Proceedings 2017, 1(4), 385; https://doi.org/10.3390/proceedings1040385.

11. Subendran, S.; Kang, C.; Chen, C. Comprehensive Hydrodynamic Investigation of Zebrafish Tail Beats in a Microfluidic Device with a Shape Memory Alloy. Micromachines 2021, 12(1), 68; https://doi.org/10.3390/mi12010068.

12. Maffiodo, D.; Raparelli, T. Flexible Fingers Based on Shape Memory Alloy Actuated Modules. Machines 2019, 7(2), 40; https://doi.org/10.3390/machines7020040.

13. Zeng, X.; Wu, Y.; Han, S.; Liu, Y.; Xiu, H.; Tian, F.; Ren, L. Theoretical and Experimental Investigations into a Crawling Robot Propelled by Piezoelectric Material. Micromachines 2021, 12(12), 1577; https://doi.org/10.3390/mi12121577.

14. Perez-Sanchez, V.; Garcia-Rubiales, F.; Nekoo, S.; Arrue, B.; Ollero, A. Modeling and Application of an SMA-Actuated Lightweight Human-Inspired Gripper for Aerial Manipulation. Machines 2023, 11(9), 859; https://doi.org/10.3390/machines11090859.

15. Raparelli T., Beomonte Zobel P., Durante F. A robot actuated by shape memory alloy wires. (2002) IEEE International Symposium on Industrial Electronics, 2, art. no. 1026323, pp. 420 - 423. DOI: 10.1109/isie.2002.1026323

16. Shin, J.; Han, Y.; Lee, J.; Han, M. Shape Memory Alloys in Textile Platform: Smart Textile-Composite Actuator and Its Application to Soft Grippers. Sensors 2023, 23(3), 1518; https://doi.org/10.3390/s23031518.

17. Shi, L.; Guo, S.; Li, M.; Mao, S.; Xiao, N.; Gao, B.; Song, Z.; Asaka, K. A Novel Soft Biomimetic Microrobot with Two Motion Attitudes. Sensors 2012, 12(12), 16732-16758; https://doi.org/10.3390/s121216732.

18. Rajagopalan, R.; Petruska, A.; Howard, D. A Bi-State Shape Memory Material Composite Soft Actuator. Actuators 2022, 11(3), 86; https://doi.org/10.3390/act11030086.

19. Maffiodo D., Raparelli T. Three-fingered gripper with flexure hinges actuated by shape memory alloy wires (2017) International Journal of Automation Technology, 11 (3), pp. 355 - 360. DOI: 10.20965/ijat.2017.p0355

20. Braun, D.; Weik, D.; Elsner, S.; Hunger, S.; Werner, M.; Drossel, W. Position Control and Force Estimation Method for Surgical Forceps Using SMA Actuators and Sensors. Materials 2021, 14(17), 5111; https://doi.org/10.3390/ma14175111.

21. Kim, H.; Jang, S.; Do, P.; Lee, C.; Ahn, B.; Kwon, S.; Chang, H.; Kim, Y. Development of Wearable Finger Prosthesis with Pneumatic Actuator for Patients with Partial Amputations. Actuators 2023, 12(12), 434; https://doi.org/10.3390/act12120434.

22. Deng, E.; Tadesse, Y. A Soft 3D-Printed Robotic Hand Actuated by Coiled SMA. Actuators 2021, 10(1), 6; https://doi.org/10.3390/act10010006.

23. Kotb, Y.; Elgamal, I.; Serry, M. Shape Memory Alloy Capsule Micropump for Drug Delivery Applications. Micromachines 2021, 12(5), 520; https://doi.org/10.3390/mi12050520.

24. Shen, J.; Chen, Y.; Sawada, H. A Wearable Assistive Device for Blind Pedestrians Using Real-Time Object Detection and Tactile Presentation. Sensors 2022, 22(12), 4537; https://doi.org/10.3390/s22124537.

25. Copaci, D.; Serrano, D.; Moreno, L.; Blanco, D. A High-Level Control Algorithm Based on sEMG Signalling for an Elbow Joint SMA Exoskeleton. Sensors 2018, 18(8), 2522; https://doi.org/10.3390/s18082522.

26. He, J.; Lu, Y.; Wang, L.; Ma, N. On the Improvement of Thermal Protection for Temperature-Responsive Protective Clothing Incorporated with Shape Memory Alloy. Materials 2018, 11(10), 1932; https://doi.org/10.3390/ma11101932.

27. Srivastava, R.; Alsamhi, S.; Murray, N.; Devine, D. Shape Memory Alloy-Based Wearables: A Review, and Conceptual Frameworks on HCI and HRI in Industry 4.0. Sensors 2022, 22(18), 6802; https://doi.org/10.3390/s22186802.

28. Lee, J.; Han, M. Design and Evaluation of Smart Textile Actuator with Chain Structure. Materials 2023, 16(16), 5517; https://doi.org/10.3390/ma16165517.

29. Helps, T.; Vivek, A.; Rossiter, J. Characterization and Lubrication of Tube-Guided Shape-Memory Alloy Actuators for Smart Textiles. Robotics 2019, 8(4), 94; https://doi.org/10.3390/robotics8040094.

30. Ameduri, S.; Concilio, A.; Favaloro, N.; Pellone, L. A Shape Memory Alloy Application for Compact Unmanned Aerial Vehicles. Aerospace 2016, 3(2), 16; https://doi.org/10.3390/aerospace3020016.

31. Bovesecchi, G.; Corasaniti, S.; Costanza, G.; Tata, M. A Novel Self-Deployable Solar Sail System Activated by Shape Memory Alloys. Aerospace 2019, 6(7), 78; https://doi.org/10.3390/aerospace6070078.

32. Liu, M.; Wang, Z.; Ikeuchi, D.; Fu, J.; Wu, X. Design and Simulation of a Flexible Bending Actuator for Solar Sail Attitude Control. Aerospace 2021, 8(12), 372; https://doi.org/10.3390/aerospace8120372.

33. Costanza, G.; Delle Monache, G.; Tata, M.; Filosi, S. Development of SMA Spring Linear Actuator for an Autonomous Lock and Release Mechanism: Application for the Gravity-Assisted Pointing System in Moon

to Earth Alignment of Directional Devices. Aerospace 2022, 9(11), 735; https://doi.org/10.3390/aerospace9110735.

34. Dimino, I.; Vendittozzi, C.; Reis Silva, W.; Ameduri, S.; Concilio, A. A Morphing Deployable Mechanism for Re-Entry Capsule Aeroshell. Appl. Sci. 2023, 13(5), 2783; https://doi.org/10.3390/app13052783.

35. Kurzawa M., Stachowiak D. Investigation on thermo-mechanical behavior of shape memory alloy actuator (2017) Archives of Electrical Engineering, 66 (4), pp. 751 - 760. DOI: 10.1515/aee-2017-0057

36. Gedouin P.-A., Pino L., Bourgeot J.-M., Delaleau E., Arbab Chirani S., Calloch S.Thermo-mechanical modelling of spring-based SMA actuators(2016). 2016 11th France-Japan and 9th Europe-Asia Congress on Mechatronics, MECATRONICS 2016 / 17th International Conference on Research and Education in Mechatronics, REM 2016, art. no. 7547171, pp. 373 - 378. DOI: 10.1109/MECATRONICS.2016.7547171

37. Lara-Quintanilla A., Bersee H.E.N. A study on the contraction and cooling times of actively cooled shape memory alloy wires(2016). Journal of Intelligent Material Systems and Structures, 27 (3), pp. 403 - 417. DOI: 10.1177/1045389X15595124

38. Raparelli T., Beomonte Zobel P., Durante F. Mechanical design of a 3-dof parallel robot actuated by smart wires. (2009) Proceedings of EUCOMES 2008 - The 2nd European Conference on Mechanism Science, pp. 271 - 278. DOI: 10.1007/978-1-4020-8915-2_33

39. Josephine Selvarani Ruth D., Sunjai Nakshatharan S., Dhanalakshmi D. Differential resistance feedback control of a self-sensing shape memory alloy actuated system. (2014) ISA Transactions, 53 (2), pp. 289 - 297. DOI: 10.1016/j.isatra.2013.11.002

40. Ruth D.J.S., Dhanalakshmi K., Nakshatharan S.S. Bidirectional angular control of an integrated sensor/actuator shape memory alloy based system. (2015) Measurement: Journal of the International Measurement Confederation, 69, pp. 210 - 221. DOI: 10.1016/j.measurement.2015.02.058

41. Josephine Selvarani Ruth J.S.R., Dhanalakshmi K. Shape memory alloy wire for self-sensing servo actuation. (2017) Mechanical Systems and Signal Processing, 83, pp. 36 - 52. DOI: 10.1016/j.ymssp.2016.05.042

42. Lan C.-C., Fan C.-H. An accurate self-sensing method for the control of shape memory alloy actuated flexures. (2010) Sensors and Actuators, A: Physical, 163 (1), pp. 323 - 332. DOI: 10.1016/j.sna.2010.07.018

43. Maffiodo D., Raparelli T. Resistance feedback of a shape memory alloy wire (2016) Advances in Intelligent Systems and Computing, 371, pp. 97 - 104. DOI: 10.1007/978-3-319-21290-6_10.

44. Raparelli T., Zobel P.B., Durante F. Design of a parallel robot actuated by shape memory alloy wires. (2002) Materials Transactions, 43 (5), pp. 1015 - 1022. DOI: 10.2320/matertrans.43.1015

45. Shi Z., Wang T., Liu D., Ma C., Yuan X. A fuzzy PID-controlled SMA actuator for a two-DOF joint. (2014) Chinese Journal of Aeronautics, 27 (2), pp. 453 - 460. DOI: 10.1016/j.cja.2014.02.015.

46. Wang, T.; Shi, Z.; Liu, D.; Ma, C.; Zhang, Z. An Accurately Controlled Antagonistic Shape Memory Alloy Actuator with Liu, S.; Huang, T.; Yen, J. Tracking Control of Shape-Memory-Alloy Actuators Based on Self-Sensing Feedback and Inverse Hysteresis Compensation. Sensors 2010, 10(1), 112-127; https://doi.org/10.3390/s100100112.